RSC Advances

PAPER

View Article Online
View Journal | View Issue

Cite this: *RSC Adv.*, 2022, **12**, 28463

Received 26th August 2022
Accepted 27th September 2022

DOI: 10.1039/d2ra05351a

rsc.li/rsc-advances

Morphology-controlled synthesis of MoS_2 using citric acid as a complexing agent and self-assembly inducer for high electrochemical performance†

Mingmin Bai, *[a] Weixin Li,[b] Hu Yang,[a] Weixia Dong,[a] Qinyu Wang[a] and Qibing Chang[a]

Two-dimensional MoS_2 with a controllable morphology was prepared *via* a simple one-step hydrothermal method. Citric acid was used as a complexing agent and self-assembly inducer. The morphology of MoS_2 changed from clusters to nanosheets, and, eventually, to stacked nanorods. A formation mechanism is proposed for the observed evolution of the morphology. The nanosheet structure presents a relatively large specific surface area, more exposed active sites and greater 1T phase content compared to the other morphologies. The electrochemical performance tests show that the MoS_2 nanosheets exhibit excellent electrochemical behavior. Their specific capacitance is 320.5 F g^{-1}, and their capacitance retention is up to 95% after 5000 cycles at 5 mA cm^{-2}. This work provides a feasible approach for changing the morphology of MoS_2 for high efficiency electrode materials for supercapacitors.

Introduction

Supercapacitors have attracted intense attention due to their excellent attributes, such as high power density, fast charge/discharge rates, and higher magnitudes of energy density. Supercapacitors are considered to be the best option for storing renewable energy.[1–3] Suitable electrode materials are important for achieving high-performance supercapacitors. To date, a number of materials have been developed for use as electrode materials in supercapacitors.[4–8]

MoS_2 is a common electrode material in supercapacitors. It can provide two-dimensional permeable channels for ion adsorption and transport, which is attributed to weak interlayer van der Waals interactions between the individual molecular layers.[9] In application, the influence of the morphology of MoS_2 on the resulting performance cannot be ignored. In the past decades, various types of MoS_2 nanostructures, including nanosheets,[10] quantum dots,[11] nanoflowers,[12] and nanomeshes,[13] have been fabricated. Among these nanostructures, layered MoS_2 nanosheets are expected to act as excellent electrode materials due to their significantly enlarged specific surface areas.

Many works have reported attempts to prepare nanosheet MoS_2. Alkali-metal intercalation–exfoliation[14] and CVD[15] are considered to be effective preparation methods for the synthesis of nanosheet MoS_2. However, these approaches are complex and difficult to use in the fabrication of large-scale devices because of their low yields. The hydrothermal method is a common method for preparing MoS_2, but the MoS_2 prepared by this method is clustered and poorly dispersed, which reduces the specific surface area and active sites of MoS_2.[16,17] Therefore, surfactants or template agents are selectively added to the solvent to improve the agglomeration or change the morphology of MoS_2.

Citric acid is a common organic acid and is often used as complexing agent or capping agent.[18] For example, F. A. Deorsola *et al.*[19] synthesized MoS_2 *via* a hydrothermal method and added citric acid as a reductant/complexing agent to obtain MoS_2 nanoparticles for lubricant applications. X. D. Zheng *et al.*[20] prepared MoS_2 with flower-like hollow microsphere and blocky structures with citric acid as a surfactant.

In addition to its morphology, the phase composition of MoS_2 is also crucial to its electrochemical performance. The metastable trigonal phase (1T) of MoS_2 presents excellent conductivity and electrochemical properties.[21] In the process of preparing MoS_2 *via* a hydrothermal method as mentioned above, it has been proved that MoS_2 with a high 1T phase content can be prepared without introducing any surfactant.[22] However, the introduction of a surfactant will affect the crystallinity of the MoS_2, and the content of the 1T phase will be reduced. Determining how to manage the trade-off between nanosheet morphology and high 1T phase content is an area that requires attention.

Herein, we report a novel approach for the controlled synthesis of high-1T-phase MoS_2 clusters, nanosheets and nanorods with citric acid as a complexing agent and self-

---

[a] *School of Materials Science and Engineering, Jingdezhen Ceramic University, Jingdezhen, 333403, PR China. E-mail: bellebai2010@126.com*

[b] *Department of Humanities, Jingdezhen University, Jingdezhen, 333499, PR China*

† Electronic supplementary information (ESI) available. See https://doi.org/10.1039/d2ra05351a

assembly inducer. It involves an easy and economical one-pot hydrothermal method for the preparation of morphology-controlled MoS_2. The experimental results show that the MoS_2 nanosheets have the best electrochemical performance because of their sufficient exposed active sites. The specific capacitance of the MoS_2 nanosheets is 320.5 F g^{-1}, and their capacitance retention is up to 95% after 5000 cycles at 5 mA cm^{-2}. This work may attract the attention of peers regarding the role of citric acid in the synthesis of nano-powder and provide an idea for the fabrication of MoS_2 nanomaterials.

Experimental

Synthesis of different morphologies of MoS_2

MoS_2 was synthesized *via* a one-step hydrothermal method using ammonium molybdate ($(NH_4)_6Mo_7O_{24}\cdot 4H_2O$) and thiourea as the molybdenum and sulfur sources. First, 2.472 g of ammonium molybdate and 2.394 g thiourea were dissolved in 40 mL deionized water, and different amounts of citric acid (0, 0.005, 0.015, 0.02, and 0.03 mol, respectively) were added to the transparent solution. After 0.5 h of stirring, the transparent solution was transferred to a 100 mL Teflon-lined reactor and reacted at 200 °C for 24 h. After being cooled to room temperature, the black products were vacuum-filtered and washed with deionized water and ethanol. Finally, the black products were dried at 70 °C for 5 h and labelled as MoS_2-CA(No.), in which CA means citric acid and No. is the number of moles of citric acid. For example, MoS_2-CA(0.02) means the sample prepared using 0.02 mol citric acid.

Characterization

The XRD data of the MoS_2 samples were collected using a Rigaku D/max-(β) X-ray diffractometer with a graphite monochromator and Cu Kα radiation ($\lambda = 0.15418$ nm) with a scanning range (2θ) of 5–80°. The microstructure and morphology of the samples were observed using a scanning electronic microscope (SEM, JEOM-JMS-6700F, Japan) and a transmission electron microscope (TEM) as well as high resolution TEM (HRTEM) (Titan G260-300). The Raman spectra of the samples were recorded using a Raman spectrometer (HR800, HoribaJobinYvon). The X-ray photoelectron spectroscopy tests were performed using a Thermo Scientific K-Alpha equipped with PerkinElmer instruments using an Al Kα monochromatic X-ray source. The photoelectron spectra were calibrated according to the binding energy of C1s at 284.5 eV. The specific surface areas of the MoS_2 samples were determined using the Brunauer–Emmett–Teller (BET) method, and the pore sizes were determined with the Barrett–Joyner–Halenda (BJH) method using the nitrogen desorption branches of the isotherms measured at 77 K (Micromeritics TriStar II 3020). Infrared spectra of the samples were recorded using a Nicolet Nexus 470 FT-IR spectrometer.

The electrochemical performances of the MoS_2 samples were tested using a three-electrode workstation (CHI660E, Shanghai Chenhua Instruments) at room temperature. 80 wt% MoS_2, 10 wt% acetylene black and 10 wt% polyvinylidene difluoride (PVDF, Aldrich) were mixed uniformly and spread onto a nickel foam substrate with a size of 1.5 × 1.5 cm to prepare the working electrodes. The active materials loaded on the substrate weighed about 1–1.5 mg per cm^2 per electrode. A platinum plate was used as a counter electrode and a saturated calomel electrode (SCE) as a reference electrode. 3 M KOH was chosen as the aqueous electrolyte solution. The CV curves were measured between −1.0 V and −0.3 V (*vs.* SCE). The galvanostatic charge/discharge (GCD) curves were recorded at 5 mA cm^{-2}, 10 mA cm^{-2}, 30 mA cm^{-2} and 50 mA cm^{-2}.

Results and discussion

In this work, different morphologies of MoS_2 were obtained by adjusting the amount of citric acid. Fig. 1 shows the SEM images of the samples synthesized with different mole contents

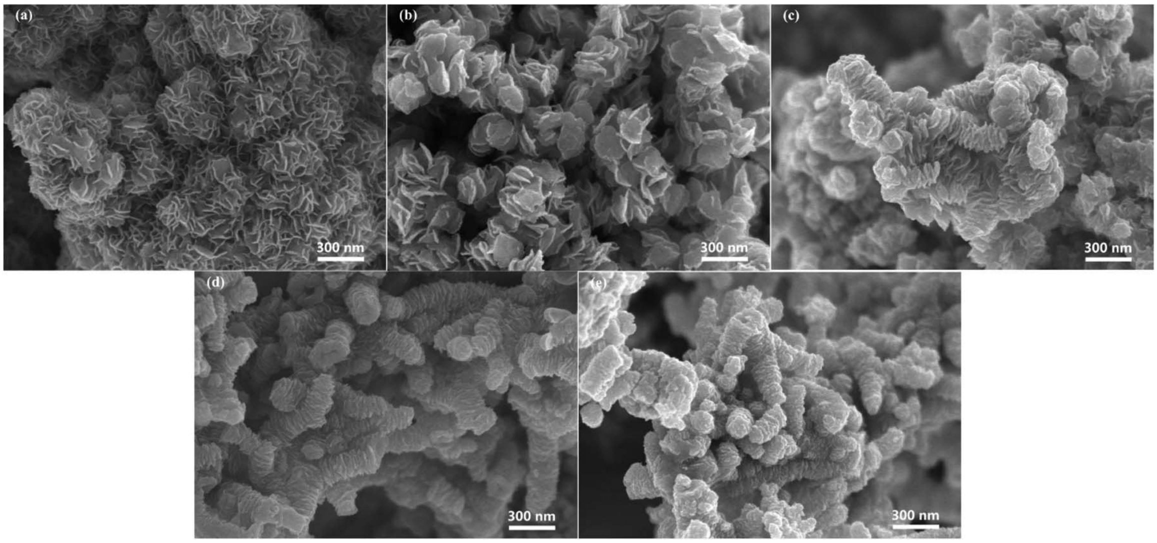

Fig. 1 SEM images of (a) MoS_2-CA(0), (b) MoS_2-CA(0.005), (c) MoS_2-CA(0.015), (d) MoS_2-CA(0.02), and (e) MoS_2-CA(0.03).

of citric acid. As presented in Fig. 1a, MoS_2-CA(0) without citric acid shows a flower-like morphology, as has been reported elsewhere.[23,24] When the citric acid content is 0.005 mol, the resulting MoS_2-CA(0.005) is no longer clustered and forms MoS_2 nanosheets (Fig. 1b). The size of the MoS_2 nanosheets is about 250 nm. As the citric acid content is increased to 0.015 mol, the resulting MoS_2-CA(0.015) nanosheets show orderly stacking and begin to form self-assembled nanorods (Fig. 1c); the nanosheets of MoS_2 are approximately 150 nm. With further increasing the citric acid content, the order of the MoS_2 nanosheet stacking gradually increases (Fig. 1d and e). As presented in Fig. S1,† a hole is observed in the cross section of some MoS_2-CA(0.02), and hollow nanorod structure is observed. The size of the nanosheets is about 100–150 nm. Fig. S2† shows that the MoS_2-CA(0.03) nanorods are composed of small nanoparticles, and the size of the nanoparticles decreases to 80 nm. This demonstrates that the addition of citric acid will induce directional self-arrangement of MoS_2 and reduce its size from nanosheets to nanoparticles.

Fig. 2 shows the TEM images, corresponding SAED patterns, and HRTEM images of the MoS_2-CA samples. Fig. 2a reveals that the curved nanosheets of MoS_2-CA(0) stacked into a flower-like structure. The HRTEM image (Fig. 2b) shows that the interlayer spacings are about 0.9 nm and 0.24 nm, corresponding to (002) and (100).[25,26] It can be seen that the 1T phase coexists with the 2H phase in a basal plane, suggesting atomic lateral heterostructures in MoS_2.[27] The diffraction rings in the selected area electron diffraction patterns (Fig. 2c) correspond to the (100), (103), and (110) planes,[25] demonstrating that polycrystalline MoS_2 was obtained. Fig. 2d shows that the MoS_2-CA(0.005)

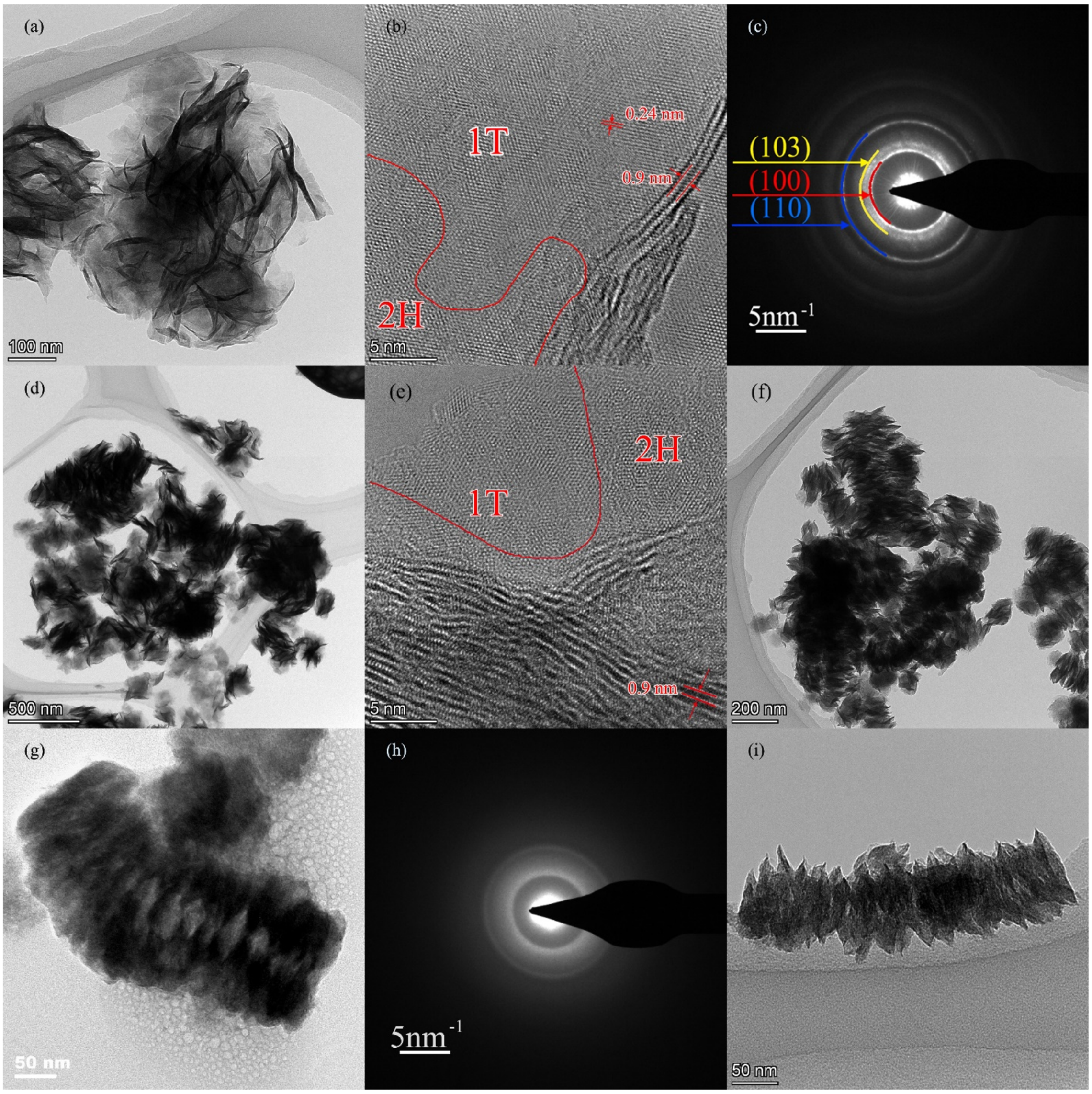

Fig. 2 (a) TEM image of MoS_2-CA(0), (b) HRTEM image of MoS_2-CA(0), and (c) the corresponding SAED diffraction pattern of MoS_2-CA(0). (d) and (e) TEM and HRTEM images of MoS_2–CA(0.005). (f) TEM image of MoS_2–CA(0.015). (g) and (h) TEM image and SAED diffraction pattern of MoS_2-CA(0.02). (i) TEM image of MoS_2–CA(0.03).

sample exhibits irregular nanosheets. From the HRTEM image of MoS_2-CA(0.005) (Fig. 2e), the interlayer spacing of (002) is about 0.9 nm, and coexistence of the 1T phase and 2H phase can also be observed. Fig. 2f reveals that the MoS_2-CA(0.015) nanosheets stack regularly into rods, and that certain gaps can be observed between the nanosheets, which present a loose stacking. For a CA content of 0.02 mol, a hollow nanorod of MoS_2 was selected; the TEM image shows a hollow rod that consists of stacked circular nanosheets (Fig. 2g). The SAED pattern (Fig. 2h) reveals distinct diffraction rings and/or bright ambiguous areas, indicating the existence of both polycrystalline and amorphous components in the sample.[28] This demonstrates that increasing the citric acid content makes MoS_2 tend to be amorphous. Fig. S3† reveals the coexistence of the 1T and 2H phases in MoS_2-CA(0.02), which proves that citric acid does not change the phase of MoS_2. Fig. 2i reveals a regular dense nanorod structure for MoS_2-CA(0.03), which corresponds with the SEM image (Fig. 1e).

Fig. 3a presents the XRD patterns of all the samples. As depicted in Fig. 3a, compared with the standard card no. 73-1539, the typical (002) peaks are located at 9.2°, indicating an interlayer expansion. The interlayer spacing calculated using the Scherrer equation is about 0.95 nm, which is close to the observed value in the HRTEM images (Fig. 2b and e), and represents an enlargement of about 0.33 nm compared to the theoretical value of 0.62 nm. The expansion should be ascribed to the intercalation of ammonium ions (NH_4^+) with a radius of 0.35 nm.[29–31] The ammonium ions should come from the raw material $(NH_4)_6Mo_7O_{24}$. The intensity of the diffraction peaks decreases with the addition of CA, especially for MoS_2-CA(0.005) and MoS_2-CA(0.015). This result illustrates that the citric acid has a negative effect on the crystallinity of MoS_2, which can be proven by the SAED pattern of MoS_2-CA(0.02) (Fig. 2h).

Fig. 3b presents the FTIR spectra of all the MoS_2-CA samples. The vibrational modes at ~3138 and 1670 cm^{-1} were assigned to the stretching vibration and bending vibration of H_2O absorbed on the MoS_2 nanosheets.[32,33] The peaks observed at 1595 cm^{-1} were attributed to the presence of COO.[34,35] The vibrational peaks at 1403 cm^{-1} should be assigned to the ammonium group.[29,36] Furthermore, the vibration modes in the region 1203–1031 cm^{-1} were attributed to the stretching modes of C–OH.[34,35] Additionally, the peaks at 912 and 760 cm^{-1} could be attributed to the Mo–O stretching vibration in MoO_3, illustrating that part of the MoS_2 was oxidized.[37,38] The weak peak at 455 cm^{-1} corresponds to the characteristic vibrational mode of Mo–S in MoS_2.[33,38] The amount of citric acid did not affect the functional groups on the surface of MoS_2.

The Raman spectra of MoS_2 are shown in Fig. 3c. It can be observed that there are five peaks at 405, 377, 335, 284 and 236 cm^{-1}. The characteristic peaks at 284 cm^{-1} (E_{1g}), 377 cm^{-1} (E^1_{2g}) and 405 cm^{-1} (A_{1g}) correspond to 2H MoS_2.[39,40] Additionally, the vibration peaks emerging at 236 cm^{-1} (J_2) and 335 cm^{-1} (J_3) are attributed to the superlattice distortion in the basal plane of the 1T phase of MoS_2,[41] suggesting the coexistence of the 1T phase and 2H phase in all samples. This proved that MoS_2 with the 1T phase can be synthesized *via* the simple one-step hydrothermal method in this paper.

Energy-dispersive X-ray spectroscopy (EDX) mappings of MoS_2-CA(0.02) were taken from the area shown in Fig. 4, and illustrate the uniform distribution of Mo, S and N in MoS_2. The element N is considered to be derived from NH_4^+.

The phase identification of the synthesized MoS_2-CA(0) and MoS_2-CA(0.02) was further studied by X-ray photoelectron spectroscopy. The two polymorphs of MoS_2 can be identified from the XPS of the Mo 3d and S 2p regions, as shown in Fig. 5. As shown in Fig. 5a and d, there are four peaks at 225.1, 228, 231, and 235.5 eV. The peak at 235.5 eV is due to the Mo $3d_{5/2}$ of Mo^{6+}, which is derived from the oxidation of Mo^{4+} in the air atmosphere.[42] The peak centered at 225.1 eV is due to S 2s in MoS_2.[16] According to the literature,[43–45] the binding energy of 1T-MoS_2 is lower than that of 2H-MoS_2. The peaks at 232.4 and 228.5 eV represent the binding energies of Mo $3d_{3/2}$ and Mo $3d_{5/2}$ for 2H-MoS_2,[30] while the peaks at 231.1 and 227.8 eV correspond to the Mo 3d binding energy of 1T-MoS_2.[46] Similarly, the S 2p peaks of 1T-MoS_2 are located at ~160.5 and ~162 eV, corresponding to S $2p_{3/2}$ and S $2p_{1/2}$, respectively. The corresponding S 2p peaks in 2H-MoS_2 are centered at ~161 and ~163.3 eV, which are slightly higher energies than those for 1T-MoS_2 (Fig. 5b and e).[47] The XPS results further demonstrate the co-existence of the 1T phase and 2H phase in MoS_2-CA(0) and MoS_2-CA(0.02). Based on the deconvolution of the Mo 3d and S 2p regions in the MoS_2-CA(0) and MoS_2-CA(0.02) spectra, the relative contents of the 1T phase were estimated to be 69.1% and 49.2%, respectively. In this paper, MoS_2 with a high content of the 1T phase was prepared *via* a simple hydrothermal method. From the estimated data, the addition of citric acid

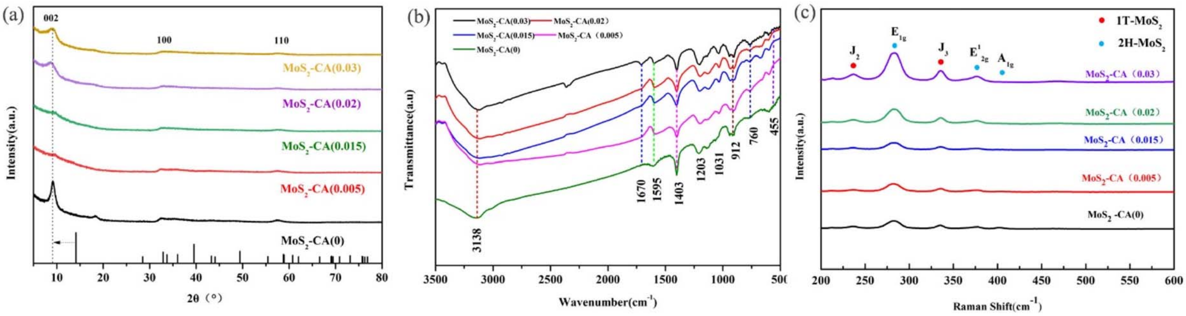

Fig. 3 (a) XRD patterns of MoS_2-CA, (b) FT-IR spectrum of MoS_2-CA, and (c) Raman spectra of MoS_2-CA.

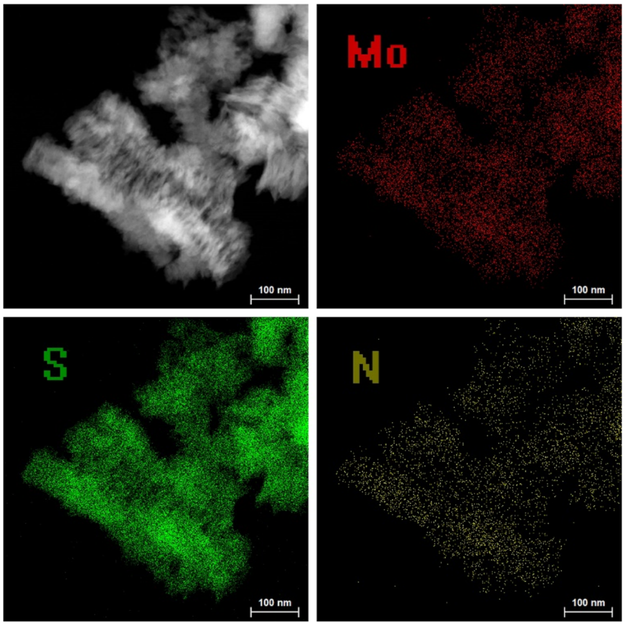

Fig. 4 EDX elemental mapping of Mo, S, and N in MoS_2-CA(0.02).

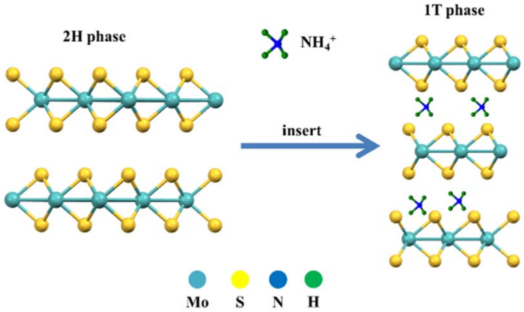

Fig. 6 The process of phase engineering.

decreases the content of the 1T phase in MoS_2-CA(0.02). Fig. 5c and f show the characteristic peaks of N 1s for MoS_2-CA(0) and MoS_2-CA(0.02), demonstrating the presence of the element N. The peak located at ~401 eV should be attributed to the intercalation of NH_4^+,[29,30] which is consistent with the XRD and EDS results.

The formation mechanism of the 1T phase of MoS_2 could be related to the insertion of NH_4^+ in the lattice (see Fig. 6). NH_4^+, which has a large radius, enlarges the interlayer distance (see Fig. 2b and e), leading to a distortion in the 2H phase. This kind of distortion would provide the driving energy for the emergence of the 1T phase. Dezhi Wang *et al.* discovered this phenomenon when ammonia or ammonium bicarbonate was added to the solution.[29,30]

Fig. 7 depicts the mechanism by which citric acid controls the morphology of MoS_2. The hydrolysis and reaction of $(NH_4)_2MoO_4$ and CH_4N_2S resulted in the formation of MoS_2. During the hydrothermal process, the reaction is usually rapid, and MoS_2 rapidly grows into clusters at the crystal nuclei that are initially formed. When citric acid is added, it acts as a complexing agent, stabilizing the metal species *via* the formation of metal citrate complexes[48] and preventing the interaction between the Mo atoms and S atoms. This effect leads to deterioration of the crystallinity of MoS_2, as observed in the XRD patterns, and slowing of the growth rate of MoS_2.[49,50] The effect of complexation on size is more obvious, and the size of nanosheets decreases from 250 nm to 80 nm (see Fig. 1). At the same time, citric acid acts as a self-assembly inducer. Citric acid has three carboxyl (–COOH) groups, and these three –COOH functional groups may also selectively bind onto the

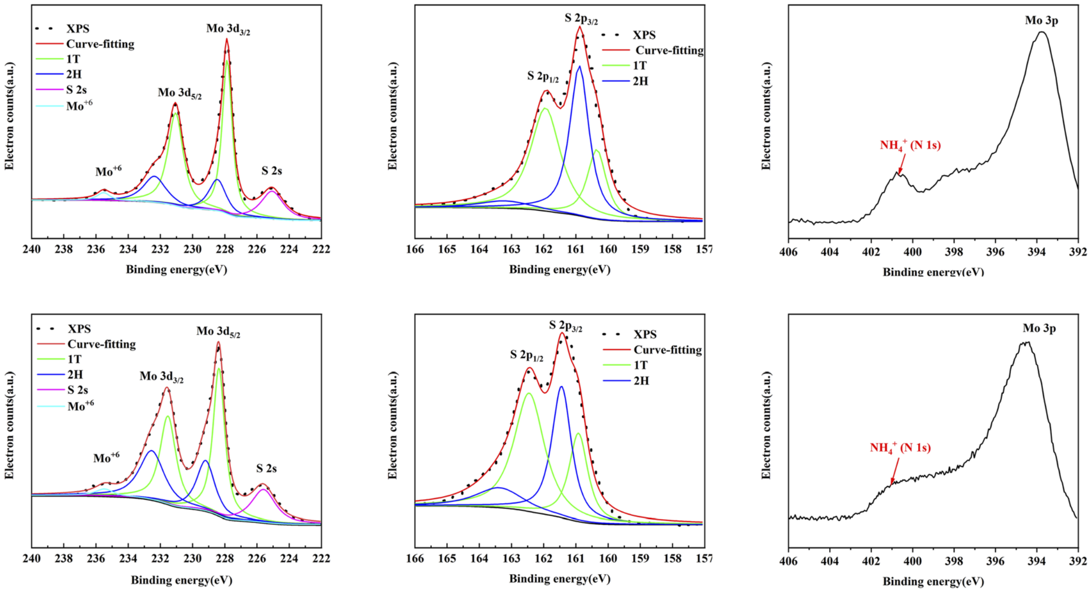

Fig. 5 XPS spectra: (a) Mo 3d of MoS_2-CA(0), (b) S 2p of MoS_2-CA(0), (c) N 1s of MoS_2-CA(0), (d) Mo 3d of MoS_2-CA(0.02), (e) S 2p of MoS_2-CA(0.02), and (f) N 1s of MoS_2-CA(0.02).

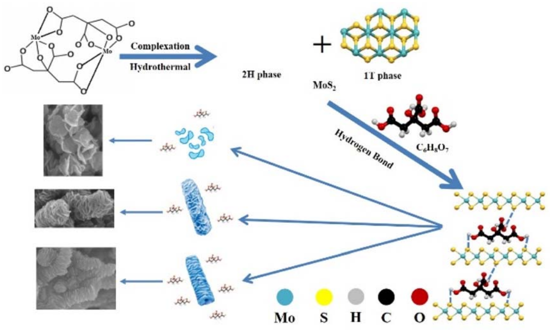

Fig. 7 Diagram of the mechanism by which citric acid controls the morphology of MoS_2.

planes of MoS_2 and form hydrogen bonding between hydrogen and sulfur.

When the amount of citric acid added is 0.005 mol, there is not enough citric acid to complex with the Mo atoms and prevent the growth of MoS_2. Additionally, the hydrogen bonds between citric acid and nanosheets are weak, so MoS_2 nanosheets are formed. With increasing the citric acid to 0.015 mol, the size of the obtained nanosheets decreases, and due to the strong hydrogen bonding, the nanosheets self-assemble into nanorods with warping and distortion (Fig. 2f). With further increasing the citric acid, the hydrogen bonding effect becomes more obvious, and MoS_2 finally stacks to form a regular rod shape. From the SEM and TEM images, the size of MoS_2-CA(0.03) is about 80 nm. Regular nanorods are obtained by the synergistic effect of hindrance and hydrogen bonding.

The adsorption–desorption isotherms and pore size distribution curves of MoS_2-CA are shown in Fig. 8. Fig. 8a–e shows that the BET surface areas of MoS_2-CA(0), MoS_2-CA(0.005), MoS_2-CA(0.015), MoS_2-CA(0.02) and MoS_2-CA(0.03) were 13.81 $m^2\ g^{-1}$, 21.89 $m^2\ g^{-1}$, 12.63 $m^2\ g^{-1}$, 13.05 $m^2\ g^{-1}$ and 30.20 $m^2\ g^{-1}$, respectively. The BET surface area of MoS_2-CA(0.005) was higher than that of MoS_2-CA(0); this effect is due to the addition of citric acid, which changes the stacking form of MoS_2. MoS_2-CA(0.005) exhibits a nanosheet structure and has more surfaces. As the amount of citric acid increased, the surface areas of MoS_2-CA(0.015) and MoS_2-CA(0.02) decreased. This can be attributed to the increase in hydrogen bonding between MoS_2 nanosheets, and the MoS_2 gradually stacked from the nanosheet structure into a rod shape. Some MoS_2 nanosheets are covered by adjacent MoS_2 nanosheets, reducing the specific surface area. MoS_2-CA(0.03) has the largest surface area, which is due to the smaller size of the MoS_2 nanoparticles. The adsorption–desorption isotherms have H3 hysteresis loops, which is a typical loop with unevenly distributed holes. Therefore, the obtained pore diameter represents slit holes formed by the accumulation of nanosheets. The BJH adsorption average pore diameters of MoS_2-CA(0), MoS_2-CA(0.005), MoS_2-CA(0.015), MoS_2-CA(0.02) and MoS_2-CA(0.03) were 25.76 nm, 27.52 nm, 25.20 nm, 28.30 nm and 14.78 nm, respectively. The pore size of MoS_2-CA(0.015) is lower than that of MoS_2-CA(0.005) due to the close packing of MoS_2 nanosheets and small slit holes. The MoS_2-CA(0.02) has a higher pore size due to the formation of hollow nanorods (see Fig. S1† and 2g). The MoS_2-CA(0.03) has the smallest pore size due to the extensive hydrogen bonding between MoS_2 nanoparticles and smaller slit holes compared to MoS_2-CA(0.015) and MoS_2-CA(0.02). The higher level of pore diameter indicates adequate contact between the active sites and electrolyte.

To evaluate the electrochemical performance of the MoS_2-CA samples, cyclic voltammetry (CV) and galvanostatic charge–

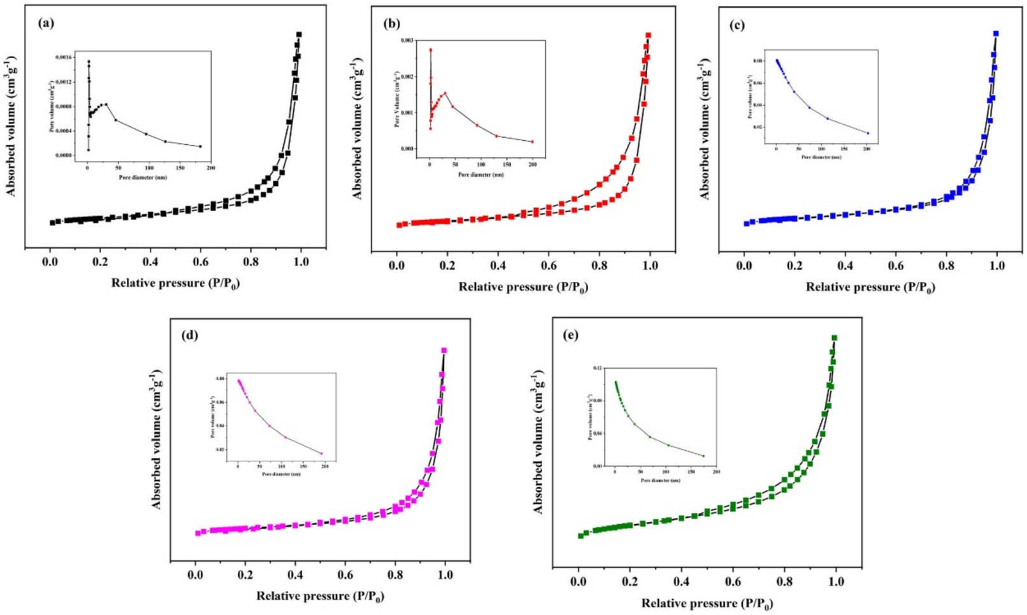

Fig. 8 N_2 adsorption–desorption isotherms and pore diameter distributions of the samples: (a) MoS_2-CA(0), (b) MoS_2-CA(0.005), (c) MoS_2-CA(0.015), (d) MoS_2-CA(0.02), and (e) MoS_2-CA(0.03).

discharge (GCD) tests were performed using three-electrode systems. Fig. 9a shows the CV curves of the MoS_2-CA samples at a scanning rate of 100 mVs^{-1} in the potential window from -1.0 to -0.3 V (*vs.* SCE). The integral area enclosed by the CV curve of the MoS_2-CA(0.005) electrode is found to be the largest of all the electrodes, showing that the MoS_2-CA(0.005) electrode has the maximum specific capacitance. This is attributed to the fact that, due to the small amount of citric acid, MoS_2 exhibits dispersed monolayer sheets, exposing more planes and boundaries able to be in contact with the electrolyte, which facilitates the ion intercalation and deintercalation reactions. The MoS_2-CA(0.015) electrode and MoS_2-CA(0) electrode have similar CV curve areas. The CV areas of MoS_2-CA(0.02) and MoS_2-CA(0.03) are smaller than that of MoS_2-CA(0). It is noteworthy that due to the large amount of citric acid, the amorphous carbon formed after hydrothermal reaction can no longer be ignored. The generated amorphous carbon reduces the conductivity of MoS_2.

Fig. 9b shows the galvanostatic charge–discharge curves of the MoS_2-CA electrodes at a current density of 5 mA cm^{-2}. There are noticeable differences among the MoS_2-CA electrodes in terms of charge–discharge time. For MoS_2-CA(0.005), the time for the charge and discharge is higher than that for MoS_2-CA(0) and MoS_2-CA(0.015), which is attributed to the high BET surface area and edge defect supplying high electrochemical activity for ion intercalation–deintercalation in electrode. In accordance with the CV results, MoS_2-CA(0.02) and MoS_2-CA(0.03) show poor charge and discharge performance. The specific capacitance based on GCD can be calculated using eqn (1):[51,52]

$$C = I\Delta t/m\Delta V \tag{1}$$

where I is the constant current density of GCD (mA cm^{-2}), Δt is the discharge time (s), m is the mass of the active material in the electrode (g), and ΔV is the potential window (V). The specific capacitances of MoS_2-CA(0), MoS_2-CA(0.005), MoS_2-CA(0.015), MoS_2-CA(0.02) and MoS_2-CA(0.03) are 268.3 F g^{-1}, 320.5 F g^{-1}, 261.9 F g^{-1}, 114.8 F g^{-1} and 112.6 F g^{-1} at a discharge current of 5 mA cm^{-2}, respectively. MoS_2-CA(0.005) shows a larger specific capacitance compared to the other electrodes, demonstrating that nanosheets are favourable for improving the energy-storage behavior of the electrode.

The specific capacitance of composites is an important performance parameter for supercapacitors.[53] Fig. 10a shows the specific capacitance of MoS_2-CA(0), MoS_2-CA(0.005) and MoS_2-CA(0.015). When the current density increased, the specific capacitance of all three samples decreased. At all current densities, the specific capacitance of MoS_2-CA(0.005) is higher than those of MoS_2-CA(0) and MoS_2-CA(0.015), which can be attributed to the fact that its dispersed single nanosheets of MoS_2 and high content of the 1T phase provide high surface area for ion transition and high conductivity between the electrode and the electrolyte. The EIS measurements of MoS_2-CA(0), MoS_2-CA(0.005) and MoS_2-CA(0.015) were performed in the frequency range of 0.01 Hz to 100 kHz at the open-circuit potential with an amplitude of 5 mV. Fig. 10b shows the Nyquist plots of the three samples. The intercept of the EIS curve at the Z' axis represents the internal resistance of the electrode and electrolyte. The diameter of the semicircle at high frequency represents the charge transfer resistance. Additionally, the straight line at low frequency relates to the Warburg impedance.[51,52,54] The impedance data of MoS_2-CA(0.005) were fitted using the software ZView to generate an equivalent electrical circuit (Fig. 10c inset). From Fig. 10b and combined with the fitting results, the internal resistance of MoS_2-CA is about 0.3 Ω, which reveals that the MoS_2-CA electrode has low internal resistance. The charge transfer resistances of MoS_2-CA(0.005) and MoS_2-CA(0.015) are approximately 0.1 Ω, which is smaller than that of MoS_2-CA(0) (0.28 Ω), which indicates that MoS_2-CA(0.005) and MoS_2-CA(0.015) exhibit favorable charge transport. In the low-frequency region, the slope of MoS_2-CA(0.005) is close to 90°, which suggests the ideal kinetic behavior of ionic diffusion.[53,54]

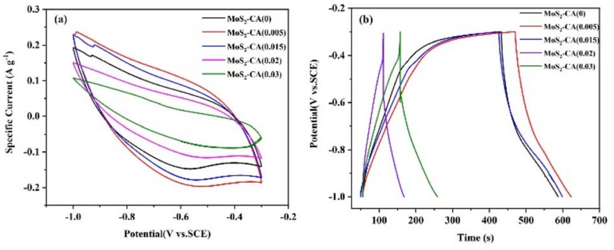

Fig. 9 (a) CV profiles at 100 mV s^{-1} and (b) GCD curves at 5 mA cm^{-2} of the as-prepared samples.

The electrochemical properties of MoS_2-CA(0.005) were further analysed. Fig. 10d shows the typical CV curves of the MoS_2-CA(0.005) electrode at different scan rates ranging from 10 mV s^{-1} to 100 mV s^{-1}. The shape of the CV curve is quasi-rectangular when the scan rate is low, showing no redox reactions. However, weak redox peaks appear in the range from -0.6 V to -0.7 V. During charging, K^+ in the electrolyte can absorb onto the surface of MoS_2 and participate in the reverse reaction process to form MoS–SK. The redox reaction can be expressed by eqn (2):

$$MoS_2 + K^+ + e^- \rightarrow MoS{-}SK \tag{2}$$

Moreover, the high content of the 1T phase in MoS_2-CA(0.005) boosts the electrochemical reaction because of the excellent conductivity of the metastable phase. The GCD curves of the MoS_2-CA(0.005) electrode are shown in Fig. 10e. The shape of the GCD curves is a quasi-isosceles triangle at high current density (30 mA cm^{-2} and 50 mA cm^{-2}), which indicates good reversibility during the charge/discharge process. At low current density, the GCD curves exhibit a near-triangle shape, and deviate slightly from linearity, which is more noticeable for the charging process. This behavior is related to the redox reaction as described in eqn (2). To further analyse the performance of MoS_2-CA(0.005) for electrochemical energy storage, its cycling stability was investigated *via* repeated charge/discharge processes at 5 mA cm^{-2}. Fig. 10f shows the cycling capacitance retention of MoS_2-CA(0.005) at 5 mA cm^{-2} over 5000 cycles. The MoS_2-CA(0.005)

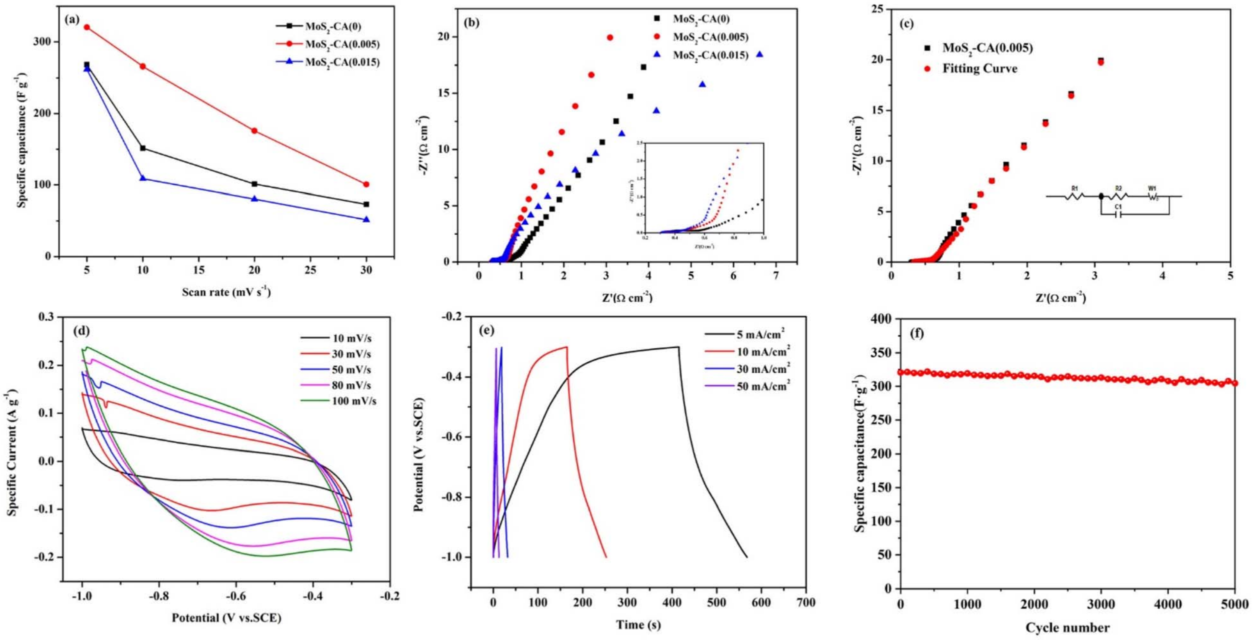

Fig. 10 (a) Specific capacitance of MoS_2-CA(0), MoS_2-CA(0.005) and MoS_2-CA(0.015) at different scan rates. (b) EIS curves of MoS_2-CA(0), MoS_2-CA(0.005) and MoS_2-CA(0.015); inset is the high-frequency region of the three samples. (c) EIS curve of MoS_2-CA(0.005) and its fitting curve; inset is the equivalent circuit for fitting. (d) CV profiles of MoS_2-CA(0.005) composites. (e) GCD curves of MoS_2-CA(0.005) composites. (f) Cycling capacitance retention of MoS_2-CA over 5000 cycles at 5 mA cm^{-2} (0.005).

Table 1 Comparison of the electrochemical properties of similar electrode materials for supercapacitors reported in the literature and the results in this paper

Electrode material	Method of preparation	Specific capacitance	Cycle life (%)	Ref
MoS_2 nanosheets	Hydrothermal	129.2 F g^{-1} @ 1 A g^{-1}	85 @ 500 cycles	55
MoS_2 nanostructure	Hydrothermal	106 F g^{-1} @ 5 mV s^{-1}	93.8 @ 1000 cycles	56
MoS_2 microspheres	Biopolymer-assisted hydrothermal	145 F g^{-1} @ 3 A g^{-1}	100 @ 500 cycles	57
3D-MoS_2 nanosheets	Hydrothermal	683 F g^{-1} @ 1 A g^{-1}	85.1 @ 10000 cycles	58
Few-layered MoS_2	Ball milling	14.7 F g^{-1} @ 0.75 A g^{-1}	91.2 @ 5000 cycles	59
MoS_2 nanoworms	Hydrothermal	138 F g^{-1} @ 1 A g^{-1}	86 @ 5000 cycles	60
MoS_2 nanosheet	Hydrothermal	320.5 F g^{-1} @ 5 mA cm^{-2}	95 @ 5000 cycles	This work

exhibits excellent cycle stability with almost 95% capacitance retention. This is attributed to the nanosheets having a high surface area and allowing abundant adsorption of ions, as well as efficient ion migration and charge transportation.

A comparison of the electrochemical properties of MoS_2 electrode materials with different morphologies used to build supercapacitors that have been reported in the literature and in this study was conducted. Compared with those in many previous reports, the MoS_2-CA(0.005) nanosheet electrode has high capacitance and long cycle life (Table 1).

Conclusion

In summary, MoS_2 with different morphologies was synthesized *via* a one-step hydrothermal method with the addition of citric acid. Flower-like cluster, nanosheet and nanorod MoS_2 were obtained. During the formation of MoS_2, citric acid acted as a complexing agent, preventing the growth and deteriorating the crystallinity of MoS_2. At the same time, the hydrogen bonding introduced by citric acid promoted the establishment of nanorods. The electrochemical properties of these structures were investigated. MoS_2-CA(0.005) exhibited the optimum electrochemical performance with a larger specific capacitance and smaller charge transfer resistance than the other MoS_2-CA composites due to its large specific surface area, more abundant exposed active sites and high 1T phase content. MoS_2-CA(0.02) and MoS_2-CA(0.03) showed poor electrochemical properties due to their low crystallinity and small specific surface area after the hydrothermal reaction with citric acid. For supercapacitors, the specific capacities of MoS_2-CA(0), MoS_2-CA(0.005), MoS_2-CA(0.015), MoS_2-CA(0.02) and MoS_2-CA(0.03) were 268.3 F g^{-1}, 320.5 F g^{-1}, 261.9 F g^{-1}, 114.8 F g^{-1} and 112.6 F g^{-1} at a current density of 5 mA cm^{-2}, respectively. This work will provide a method for the morphology design and performance modification of MoS_2 for supercapacitors.

Author contributions

Mingmin Bai: Conceptualization, Methodology, Writing – original draft, Data curation. Weixin Li: Software, Validation, Formal analysis, Visualization. Hu Yang: Investigation, Methodology, Software. Weixia Dong: Writing – review & editing. Qinyu Wang: Investigation, Methodology. Qibing Chang: Writing – review & editing.

Conflicts of interest

The authors declare no competing financial interest.

Acknowledgements

This work was financially supported by the Education Project of Jiangxi Province in China [Grant No. GJJ201301, GJJ211309], National Natural Science Foundation of China [Grant No. 51772136] and 2021 Open Project "State Key Laboratory of Silicon Materials" [Grant No. SKL2021-04].

Notes and references

1 Z. Song, L. Miao, L. Li, D. Zhu, L. Gan and M. Liu, *Carbon*, 2021, **180**, 135–145.
2 Q. Yang, M. Liang, M. Mansuer, C. M. Hu, Y. K. Lv, L. H. Gan and M. X. Liu, *ACS Appl. Mater. Interfaces*, 2022, **14**, 33328–33339.
3 Z. Y. Song, L. Miao, H. Duan, L. Ruhlmann, Y. K. Lv, D. Z. Zhu, L. C. Li, L. H. Gan and M. X. Liu, *Angew. Chem., Int. Ed.*, 2022, **61**, e202208821.
4 R. Abazari, S. Sanati, A. Morsali and D. P. Dubal, *J. Mater. Chem. A*, 2021, **9**, 11001.
5 I. S. Imaduddin, S. R. Majid, S. B. Aziz, I. Brevik, S. N. F. Yusuf, M. A. Brza, S. R. Saed and M. F. Z. A. Kadir, *Materials*, 2021, **14**, 573.
6 F. Azimov, J. Kim, S. M. Choi and H. M. Jung, *Nanomaterials*, 2021, **11**, 1557.
7 G. Singh, R. Bahadur, A. M. Ruban, J. M. Davidraj, D. Su and A. Vinu, *Green Chem.*, 2021, **23**, 5571.
8 Q. Liu, A. R Zhao, X. X. He, Q. Li, J. Sun, Z. B. Lei and Z. H. Liu, *Adv. Funct. Mater.*, 2021, **31**, 2010944.
9 O. Samy, S. Zeng, M. D. Birowosuto and A. El Moutaouakil, *Crystals*, 2021, **11**, 355.
10 D. Voiry, M. Salehi, R. Silva, T. Fujita, M. Chen, T. Asefa, V. B. Shenoy, G. Eda and M. Chhowalla, *Nano Lett.*, 2013, **13**, 6222e6227.
11 X. Li, X. Lv, N. Li, J. Wu, Y.-Z. Zheng and X. Tao, *Appl. Catal. B Environ.*, 2019, **243**, 76e85.
12 J. M. Wu, W. E. Chang, Y. T. Chang and C. K. Chang, *Adv. Mater.*, 2016, **28**, 3718e3725.
13 Y. Li, K. Yin, L. Wang, X. Lu, Y. Zhang, Y. Liu, D. Yan, Y. Song and S. Luo, *Appl. Catal. B Environ.*, 2018, **239**, 537e544.
14 X. Fan, P. Xu, Y. C. Li, D. Zhou, Y. Sun, M. A. T. Nguyen, M. Terrones and T. E. Mallouk, *J. Am. Chem. Soc.*, 2016, **138**, 5143.
15 J. Jeon, S. K. Jang, S. M. Jeon, G. Yoo, Y. H. Jang, J. H. Park and S. Lee, *Nanoscale*, 2015, **7**, 1688.
16 Y. Shi, Y. Zhou, D. R. Yang, W. X. Xu, C. Wang, F. B. Wang, J. J. Xu, X. H. Xia and H. Y. Chen, *J. Am. Chem. Soc.*, 2017, **139**, 15479.
17 M. D. Sharma, C. Mahala, B. Modak, S. Pande and M. Basu, *Langmuir*, 2021, 4847.
18 N. Reddy and Y. Yang, *Food Chem.*, 2010, **118**, 702–711.
19 F. A. Deorsola, N. Russo, G. A. Blengini and D. Fino, *Chem. Eng. J.*, 2012, **195–196**, 1–6.
20 X. Zheng, Y. Zhu, Y. Sun and J. Qingjie Jiao, *J. Power Sources*, 2018, **395**, 318–327.
21 L. N. Wang, X. Wu, F. T. Wang, X. Chen, J. Xu and K. J. Huang, *J. Colloid Interface Sci.*, 2021, **583**, 579–585.
22 C. Tan, Z. Luo, A. Chaturvedi, Y. Cai, Y. Du, Y. Gong, Y. Huang, Z. Lai, X. Zhang, L. Zheng, X. Qi and M. Hao, *Adv. Mater.*, 2018, 1705509.
23 Z. Feng, P. Yang, G. Wen, H. Li, Y. Liu and X. Zhao, *Appl. Surf. Sci.*, 2020, **502**, 144129.
24 L. Pan, C. Jiao, Y. Liang, J. Xiong, S. Wang, H. Zhu, G. Chen and H. Song, *New J. Chem.*, 2021, **45**, 5645.
25 G. Suo, J. Zhang, D. Li, Q. Yu, M. He, L. Feng, X. Hou, Y. Yang, X. Ye, L. Zhang and W. Wang, *J. Colloid Interface Sci.*, 2020, **566**, 427–433.
26 H. Xu, J. Yi, X. She, Q. Liu, L. Song, S. Chen, Y. Yang, Y. Song, R. Vajtai, J. Lou, H. Li, S. Yuan, J. Wu and P. M. Ajayan, *Appl. Catal., B*, 2018, **220**, 379.
27 W. Liu, C. Luo, S. Zhang, B. Zhang, J. Ma, X. Wang, W. Liu, Z. Li, Q. H. Yang and W. Lv, *ACS Nano*, 2021, **15**, 7491.
28 H. Ren, Z. Xiong, E. Wang, Z. Yuan, Y. Sun, K. Zhu, B. Wang, X. Wang, H. Ding, P. Liu, L. Zhang, J. Wu, S. Fan, X. Li and K. Liu, *ACS Nano*, 2019, **13**, 3106.
29 D. Wang, X. Zhang, S. Bao, Z. Zhang, H. Fei and Z. Wu, *J. Mater. Chem. A*, 2017, **5**, 2681.
30 D. Wang, B. Su, Y. Jiang, L. Li, B. K. Ng, Z. Wu and F. Liu, *Chem. Eng. J.*, 2017, **330**, 102.
31 J. Dai, Y. Lv, J. Zhang, D. Zhang, H. Xie, C. Guo, A. Zhu, Y. Xu, M. Fan, C. Yuan and L. Dai, *J. Colloid Interface Sci.*, 2021, **590**, 591.
32 A. T. Massey, R. Gusain, S. Kumari and O. P. Khatri, *Ind. Eng. Chem. Res.*, 2016, **55**, 7124–7131.
33 S. Kumari, R. Gusain, N. Kumar and O. P. Khatri, *J. Ind. Eng. Chem.*, 2016, **42**, 87.
34 A. Santra, M. Kayal, S. Tiwari, D. Jana and B. Ghosh, *J. Basic Appl. Eng. Res.*, 2015, **2**, 1309.
35 S. Mishra, P. K. Maurya and A. K. Mishra, *Mater. Chem. Phys.*, 2020, **255**, 123551.
36 Z. Guo, Q. Ma, Z. Xuan, F. Du and Y. Zhong, *RSC Adv.*, 2016, **6**, 16730.
37 L. Ye, W. Guo, Y. Yang, Y. Du and Y. Xie, *Chem. Mater.*, 2007, **19**, 6331.
38 G. Nagaraju, C. N. Tharamani, G. T. Chandrappa and J. Livage, *Nanoscale Res. Lett.*, 2007, **2**, 461.

39 J. Kibsgaard, Z. Chen, B. N. Reinecke and T. F. Jaramillo, *Nat. Mater.*, 2012, **11**, 963–969.

40 X. Fan, P. Xu, D. Zhou, Y. Sun, Y. C. Li, M. T. Nguyen, M. Terrones and T. E. Mallouk, *Nano Lett.*, 2015, **15**, 5956.

41 F. Ma, Y. Liang, P. Zhou, F. Tong, Z. Wang, P. Wang, Y. Liu, Y. Dai, Z. Zheng and B. Huang, *Mater. Chem. Phys.*, 2020, **244**, 122642.

42 B. B. Fan, H. N. Fan, X. H. Chen, X. W. Gao, S. Chen, Q. L. Tang, W. B. Luo, Y. Deng, A. P. Hu and W. Hu, *ACS Appl. Mater. Interfaces*, 2021, **13**, 19894.

43 G. Eda, H. Yamaguchi, D. Voiry, T. Fujita, M. Chen and M. Chhowalla, *Nano Lett.*, 2011, **11**, 5111.

44 M. Acerce, D. Voiry and M. Chhowalla, *Nat. Nanotechnol.*, 2015, **10**, 313–318.

45 Y. Qi, Q. Xu, Y. Wang, B. Yan, Y. Ren and Z. Chen, *ACS Nano*, 2016, **10**, 2903–2909.

46 X. Chen, Z. Wang, Y. Wei, X. Zhang, Q. Zhang, L. Gu, L. Zhang, N. Yang and R. Yu, *Agnew. Chem.*, 2019, **131**, 1.

47 H. Zhao, S. Cui, G. Li, N. Li and X. Li, *J. Colloid Interface Sci.*, 2020, **567**, 10.

48 M. Dong, J. Wang and Y. Sun, *Microporous Mesoporous Mater.*, 2001, **43**, 237.

49 B. Lertpanyapornchai, T. Yokoi and C. Ngamcharussrivichai, *Microporous Mesoporous Mater.*, 2016, **226**, 505.

50 R. Rai and M. Molli, *Bull. Mater. Sci.*, 2021, **44**, 34.

51 S. Moghimian and P. Sangpour, *J. Appl. Electrochem.*, 2020, **50**, 71.

52 J. Dai, Y. Lv, J. Zhang, D. Zhang, H. Xie, C. Guo, A. Zhu, Y. Xu, M. Fan, C. Yuan and L. Dai, *J. Colloid Interface Sci.*, 2021, **590**, 591–600.

53 A. Gigot, M. Fontana, M. Serrapede, M. Castellino, S. Bianco, M. Armandi, B. Bonelli, C. F. Pirri, E. Tresso and P. Rivolo, *ACS Appl. Mater. Interfaces*, 2016, **8**, 32842.

54 Z. Qua, M. Shia, H. Wua, Y. Liua, J. Jianga and C. Yan, *J. Power Sources*, 2019, **410**, 179.

55 A. Ramadoss, T. Kim, G. S. Kima and S. J. Kim, *New J. Chem.*, 2014, **38**, 2379.

56 C. Zhang, J. Ning, B. Wang, H. Guo, X. Feng, X. Shen, Y. Jia, J. Dong, D. Wang, J. Zhang and Y. Hao, *Nano Res.*, 2021, **14**, 114.

57 A. Laheäär, P. Przygocki, Q. Abbas and F. Béguin, *Electrochem. Commun.*, 2015, **60**, 21.

58 K. J. Huang, J. Z. Zhang, G. W. Shi and Y. M. Liu, *Electrochim. Acta*, 2014, **4**, 7.

59 K. Krishnamoorthy, G. K. Veerasubramani, S. Radhakrishnan and S. J. Kim, *Mater. Res. Bull*, 2014, **50**, 499–502.

60 L. Ma, L. M. Xu, X. P. Zhou and X. Y. Xu, *Mater. Lett.*, 2014, **132**, 291–294.